



Discontinuous Galerkin method for the computation of acoustic modes in lined flow ducts with rigid splices

Lucas Pascal, Estelle Piot, Grégoire Casalis

► To cite this version:

Lucas Pascal, Estelle Piot, Grégoire Casalis. Discontinuous Galerkin method for the computation of acoustic modes in lined flow ducts with rigid splices. *Journal of Sound and Vibration*, 2013, vol. 332 (n° 13), pp. 3270-3288. 10.1016/j.jsv.2013.01.021 . hal-01453178

HAL Id: hal-01453178

<https://hal.science/hal-01453178>

Submitted on 2 Feb 2017

HAL is a multi-disciplinary open access archive for the deposit and dissemination of scientific research documents, whether they are published or not. The documents may come from teaching and research institutions in France or abroad, or from public or private research centers.

L'archive ouverte pluridisciplinaire **HAL**, est destinée au dépôt et à la diffusion de documents scientifiques de niveau recherche, publiés ou non, émanant des établissements d'enseignement et de recherche français ou étrangers, des laboratoires publics ou privés.



Open Archive TOULOUSE Archive Ouverte (OATAO)

OATAO is an open access repository that collects the work of Toulouse researchers and makes it freely available over the web where possible.

This is an author-deposited version published in: <http://oatao.univ-toulouse.fr/>
Eprints ID: 16605

To cite this version: Pascal, Lucas and Piot, Estelle and Casalis, Grégoire Discontinuous Galerkin method for the computation of acoustic modes in lined flow ducts with rigid splices. (2013) Journal of Sound and Vibration, vol. 332 (n° 13). pp. 3270-3288. ISSN 0022-460X

Official URL: <http://dx.doi.org/10.1016/j.jsv.2013.01.021>

Any correspondence concerning this service should be sent to the repository administrator: staff-oatao@listes-diff.inp-toulouse.fr

Discontinuous Galerkin method for the computation of acoustic modes in lined flow ducts with rigid splices

L. Pascal*, E. Piot, G. Casalis

ONERA, Department of Aerodynamics and Energetics modelling, The French Aerospace Lab, F-31055 Toulouse, France

A B S T R A C T

A discontinuous Galerkin method for the discretisation of the linearised Euler equations is derived for the computation of acoustic modes in an infinite duct of arbitrary geometric shape in the presence of axial sheared flow. Validations are performed with analytical solutions in the case of a uniformly lined duct and comparisons are done with the literature in the case of a lined cylindrical duct with rigid splices. We take advantage of the discontinuous formulation to study the behaviour of the acoustic eigenfunctions in the vicinity of the liner-splice transition where singular behaviours of the acoustic perturbation are found.

1. Introduction

Inviscid stability analysis performed in a lined or unlined infinite duct in the presence of flow or not is an important tool in acoustics since it gives an insight on the physical phenomena responsible for the propagation and radiation of the noise generated by an aircraft engine. In some cases, solutions may be simply expressed through Bessel functions whereas more elaborated analytical or even numerical methods are required in most cases.

Present paper focuses on the case of a cylindrical infinite duct uniformly lined except at some “small” parts. This models the intake of an engine (see for instance [1]) where the lining is formed by joining together pieces of liners, leaving unlined areas at the joints, called splices. In addition, small areas of the lining may be replaced by hard patches for maintenance reasons. These splices may have a significant effect on the radiated noise and therefore the infinite duct model presenting lining non-uniformities or discontinuities has been already the object of many studies [2–6] by means of various methods (analytical or numerical). Except in specific cases with thin splices (see [6]), the effect of the splices is generally to reduce the damping, as it would be guessed since the lined area is smaller. Mustafi et al. [7] considered the case of a square hard patch in a uniformly lined flow duct. They showed that the relative sound power level increases with the patch width up to a width of the same magnitude as the incident mode azimuthal wavelength. Another consequence of the presence of splices is the scattering of acoustic cut-on modes into modes of different azimuthal orders. Finally, as discovered by Bi et al. [5] and studied as well by Brambley et al. [6], in the presence of rigid splices in a lined duct, a new kind of mode called “localised” mode (Brambley et al. call them “trapped” modes) may appear and is characterised by the fact that it exists only near the splices. It has been shown that a localised mode originates as a surface wave and turns into an acoustic wave as the splice width increases.

* Corresponding author. Tel.: +33 562252232.

E-mail addresses: lucas.pascal@onera.fr (L. Pascal), estelle.piot@onera.fr (E. Piot), gregoire.casalis@onera.fr (G. Casalis).

The previous investigations of circumferentially non-uniformly lined duct have been conducted by means of finite element method with [4] and without flow [2] or by means of multimodal method [3,5] in the presence of uniform flow. In these studies, the equations are written under the Pridmore–Brown form and therefore the only considered variable is the acoustic pressure. The multimodal method consists in expanding the searched solution in terms of the eigenmodes of the rigid duct case or of the uniformly lined duct case (although for this configuration, the equations are not self-adjoint). On the contrary, Brambley et al. [6] searched the eigenmodes under the form of Fourier series derived using Green's function method, which ensures the completeness of the expansion. The method they proposed may be applied to ducts of arbitrary shape in the presence of any axial flow. In a similar way, this paper presents a numerical method for computing eigenmodes in a non-uniformly lined duct of arbitrary shape and carrying axial flow with special focus on the discontinuity effect induced by the splice. In addition to be able to handle complex geometries, the numerical method is required to have low numerical dissipation and dispersion. The discontinuous Galerkin method satisfies all these requirements and is hence used for the spatial discretisation. Moreover, the method offers the capacity to easily handle discontinuities, in particular at the boundaries. The discontinuous Galerkin method has been successfully employed in the calculation of modes arising from the incompressible Navier–Stokes equations on quite complex geometries [8]. The present code is derived from an existing Computational Aeroacoustics (CAA) solver based on the discontinuous Galerkin method developed at ONERA [9].

In the literature, lining discontinuities are not restricted to splices. It mainly arises when the liner is not axially infinite, which is usually addressed by the mode matching method [10]. In [2,4], the authors considered a liner which is axially finite and contains splices in the circumferential direction. Wright [2] derived a mode-matching procedure in the usual way, in the sense that the continuity of the pressure is imposed at the lining transition. Gabard and Astley [4] proposed a more elaborated matching scheme by deriving a variational formulation from the field equations. Another technique has been used by Rienstra [11] and Brambley [12], who investigated the scattering in an infinite duct at a sudden hard–soft wall impedance transition with uniform flow by means of the Wiener–Hopf method. Although all these investigations give interesting results on the acoustics scattering, none of them really focused on the local behaviour of the perturbation at the hard–soft lining transition. Unfortunately, as pointed out by Gabard and Astley [4] “there is as yet no definite and complete description of the physical mechanisms taking place at the transition from hard to soft surfaces with flow”. Moreover, even without flow, the local behaviour of the perturbation components at the lining transition is still an open problem.

In the present paper, focus is made on the acoustic modes computation in the case of two diametrically opposed splices as in Brambley et al. [6]. Section 2 provides the detailed context and the governing equations, which are discretised by means of the discontinuous Galerkin method described in Section 3. Sections 4–6 are devoted to numerical results: in Section 4, comparisons are presented with analytical solutions available for the uniformly lined duct without flow, and comparisons are done with the published results in the configuration with rigid splices and in the presence or not of sheared flow. The numerical performance of the method is presented as well. In Section 5 is presented a deeper study on the splice effects. More particularly, the shape of the eigenfunctions in the vicinity of the lining discontinuities resulting from the presence of the splices is investigated. Finally in Section 6 is shown the flexibility of the method by considering ducts of different geometries with flow and with lining discontinuities.

2. Governing equations

The considered geometry consists of an infinite circular duct of radius R uniformly lined except at two rigid splices. The splices are located around $\theta = 0$ and $\theta = \pi$ and are $2\theta_s$ wide. The geometry is depicted in Fig. 1 together with the definitions of the Cartesian and cylindrical coordinates systems.

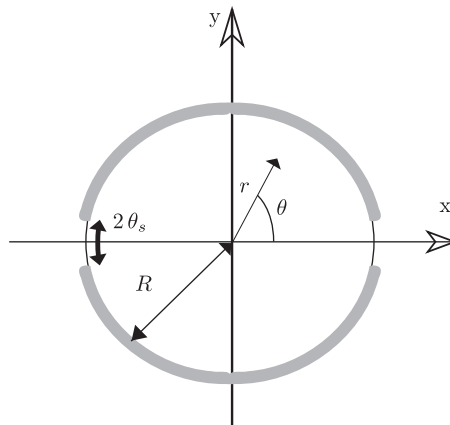


Fig. 1. Cylindrical spliced lined duct—the grey wide circular line represents the liner.

The main flow (denoted with subscript 0) is assumed to be stationary, subsonic and homentropic. Moreover the considered main flow velocity is oriented towards z and depends only on the radial coordinate r , the corresponding Mach number is denoted M_0 . Finally the mean density ρ_0 and the sound speed a_0 are taken constant. The current method may also handle more complex main flows such as in the bypass duct of a turbofan where there are density gradients and a swirl component for instance. However, the configuration chosen in this paper represents the intake of a turbofan where the main flow model is simpler.

In the following, the different quantities are made dimensionless thanks to reference quantities: a_0 for the velocity, $\rho_0 a_0^2$ for the pressure, R for the length and R/a_0 for the time.

The governing equations are the linearised Euler equations where the perturbations are taken under a wavelike form $\tilde{\Phi}(x, y, z, t) = \exp(i(kz - \omega t))\phi(x, y)$,¹ ω being the dimensionless angular frequency, k the dimensionless wavenumber and $\phi = (\mathbf{u}, p)$ the unknown vector composed of the perturbation velocity vector and the perturbation pressure. The velocity vector in Cartesian coordinates writes $\mathbf{u} = u\mathbf{e}_x + v\mathbf{e}_y + w\mathbf{e}_z$ and $\mathbf{u} = u_r\mathbf{e}_r + u_\theta\mathbf{e}_\theta + w\mathbf{e}_z$ in cylindrical coordinates. The equations are then written in Cartesian coordinates system in the domain Ω under the matrix form (the Einstein summation is used on x and y)

$$-i\omega\phi + \mathbf{A}_j\partial_j\phi + (\mathbf{B} + ik\mathbf{C})\phi = 0 \quad \text{in } \Omega \quad (1)$$

where

$$\mathbf{A}_x = \begin{pmatrix} 0 & 0 & 0 & 1 \\ 0 & 0 & 0 & 0 \\ 0 & 0 & 0 & 0 \\ 1 & 0 & 0 & 0 \end{pmatrix}, \quad \mathbf{A}_y = \begin{pmatrix} 0 & 0 & 0 & 0 \\ 0 & 0 & 0 & 1 \\ 0 & 0 & 0 & 0 \\ 0 & 1 & 0 & 0 \end{pmatrix}, \quad \mathbf{B} = \begin{pmatrix} 0 & 0 & 0 & 0 \\ 0 & 0 & 0 & 0 \\ \partial_x M_0 & \partial_y M_0 & 0 & 0 \\ 0 & 0 & 0 & 0 \end{pmatrix},$$

and

$$\mathbf{C} = \begin{pmatrix} M_0 & 0 & 0 & 0 \\ 0 & M_0 & 0 & 0 \\ 0 & 0 & M_0 & 1 \\ 0 & 0 & 1 & M_0 \end{pmatrix}.$$

The boundary conditions on the perturbation at the wall $\partial\Omega$ are imposed by means of an impedance condition modelled by Eq. (2) where Z is the specific acoustic impedance and \mathbf{n} is the outward-pointing unit normal vector:

$$p = Z\mathbf{u} \cdot \mathbf{n} \quad \text{on } \partial\Omega \quad (2)$$

But rather than using the specific impedance and Eq. (2), the reflection coefficient β defined as $\beta = (Z-1)/(Z+1)$ is introduced to avoid singular behaviour when $Z=0$ (soft wall) and $Z \rightarrow \infty$ (hard wall). The boundary conditions at the wall become

$$(\beta-1)p + (\beta+1)\mathbf{u} \cdot \mathbf{n} = 0 \quad \text{on } \partial\Omega \quad (3)$$

Finally, no-slip boundary conditions are imposed on the main flow in order to avoid any vortex-sheet on the liner.²

For a chosen dimensionless angular frequency $\omega \in \mathbb{R}^+$, the complex wavenumber k is computed as being an eigenvalue of the eigenproblem composed of Eqs. (1) and (2), ϕ being the eigenfunction.

3. Numerical method

In this section, the discontinuous Galerkin method applied to the problem formed by Eqs. (1) and (2) is briefly presented. A more detailed theoretical study may be found in [17].

The discontinuous Galerkin method is a local method: on each triangle $(D_l)_{l \in \llbracket 1, L \rrbracket}$ (see Fig. 2) of the computational domain Ω_h bordered by $\partial\Omega_h$, the solution is searched in $P^2(D_l)$, the space of second order polynomial defined on D_l . The solution is found locally by imposing a Galerkin condition (i.e. an orthogonality condition): the local residual must be orthogonal to every test-function ψ_m belonging to the space of test functions V_h^l , chosen here as being in $P^2(D_l)$:

$$\forall l \in \llbracket 1, L \rrbracket, \forall \psi_m \in V_h^l \quad \int_{D_l} (-i\omega\phi + \mathbf{A}_j\partial_j\phi + (\mathbf{B} + ik\mathbf{C})\phi) \cdot \psi_m \, dx \, dy = 0 \quad (4)$$

¹ We choose to follow the stability convention in opposition to the acoustical convention for which the exponent is $i(\omega t - kz)$. This should be kept in mind when looking at computed spectra or impedance values.

² Else the perturbations would have to satisfy the Ingard-Myers boundary condition which takes into account the dynamic of the vortex sheet over the lining [13–16].

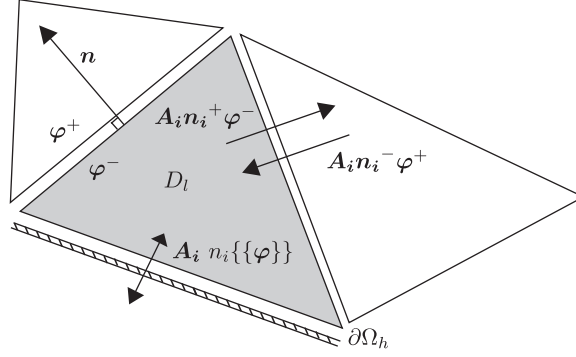


Fig. 2. Sketch of a triangle showing the interior and exterior traces and the numerical fluxes.

Integrating by parts yields

$$\forall l \in \llbracket 1, L \rrbracket, \forall \psi_m \in V_h^l \int_{D_l} (-i\omega \phi \cdot \psi_m - \partial_j(\psi_m \cdot \mathbf{A}_j) \phi + (\mathbf{B} + ik\mathbf{C}) \phi \cdot \psi_m) dx dy + \int_{\partial D_l} n_j \mathbf{A}_j \phi \cdot \psi_m d\Gamma = 0 \quad (5)$$

where $d\Gamma$ represents the unilinear differential along the boundary ∂D_l .

A particularity of the discontinuous Galerkin method is that the solution ϕ is multiply defined on ∂D_l . The concept of interior and exterior traces of the solution is then introduced, respectively denoted ϕ^- and ϕ^+ and defined as being $\phi^\pm(\mathbf{x}) = \lim_{\epsilon \rightarrow 0} \phi(\mathbf{x} \pm \epsilon \mathbf{n})$ for $\mathbf{x} \in \partial D_l$ and \mathbf{n} the vector normal to ∂D_l oriented outward from D_l (see Fig. 2). Therefore, the definition of the flux $\mathbf{A}_j n_j \phi$ becoming ambiguous, it is replaced by a numerical flux depending on the interior and exterior traces and on the normal \mathbf{n} : $\Pi(\phi^-, \phi^+, \mathbf{n})$.

If ∂D_l is the border between two triangles, the numerical flux is constructed by means of the characteristics method and therefore takes into account the dynamics of the problem. As the matrix $\mathbf{A}_j n_j$ is real and symmetric, it may be diagonalised: $\mathbf{A}_j n_j = \mathbf{P} \mathbf{\Lambda} \mathbf{P}^{-1} = \mathbf{P} \mathbf{\Lambda}^+ \mathbf{P}^{-1} + \mathbf{P} \mathbf{\Lambda}^- \mathbf{P}^{-1} = [\mathbf{A}_j n_j]^+ + [\mathbf{A}_j n_j]^-$. The matrix $\mathbf{\Lambda}^+$ (respectively $\mathbf{\Lambda}^-$) contains the positive (respectively negative) eigenvalues of $\mathbf{A}_j n_j$ and hence its components correspond to the characteristics propagating out of D_l (respectively into D_l). Finally, the resulting flux Π defined by Eq. (6) is a so-called upwind flux (as in finite volume method): “it takes the informations from where they are coming”.

$$\Pi = [\mathbf{A}_j n_j]^- \phi^+ + [\mathbf{A}_j n_j]^+ \phi^- \quad (6)$$

If ∂D_l belongs to the computational domain boundary (see Fig. 2): $\partial D_l \cap \partial \Omega_h \neq \emptyset$, the numerical flux is intended to enforce the boundary conditions. A centred flux is chosen $\Pi = \mathbf{A}_j n_j (\phi^+ + \phi^-)/2$ where the exterior trace is required to satisfy $p^+ = \beta p^- + (\beta + 1) \mathbf{u}^- \cdot \mathbf{n}$ and $\mathbf{u}^+ \cdot \mathbf{n} = (1 - \beta) p^- - \beta \mathbf{u}^- \cdot \mathbf{n}$. We checked that using this centred flux at an external boundary yields a better numerical accuracy than using the upwind flux (6).

Replacing in Eq. (5) $\mathbf{A}_j n_j \phi$ by the appropriate numerical flux and integrating by parts again yields

$$\begin{aligned} \forall l \in \llbracket 1, L \rrbracket, \forall \psi_m \in V_h^l \int_{D_l} (-i\omega \phi + \mathbf{A}_j \partial_j \phi + (\mathbf{B} + i k \mathbf{C}) \phi) \cdot \psi_m d\Omega \\ + \int_{\partial D_l \cap \partial \Omega_h} [\mathbf{A}_j n_j]^- (\phi^+ - \phi^-) \cdot \psi_m d\Gamma + \int_{\partial D_l \cap \partial \Omega_h} \mathbf{M}(\beta) \phi^- \cdot \psi_m d\Gamma = 0 \end{aligned} \quad (7)$$

where

$$\mathbf{M}(\beta) = \frac{1}{2} \begin{pmatrix} (\beta + 1)n_x^2 & (\beta + 1)n_x n_y & 0 & (\beta - 1)n_x \\ (\beta + 1)n_x n_y & (\beta + 1)n_y^2 & 0 & (\beta - 1)n_y \\ 0 & 0 & 0 & 0 \\ -(1 + \beta)n_x & -(1 + \beta)n_y & 0 & (1 - \beta) \end{pmatrix}$$

The geometry of the problem (see Fig. 1) admits the vertical axis $x=0$ and the horizontal axis $y=0$ as symmetry axes. Thanks to these symmetry properties, the computations are performed on the domain contained between $\theta=0$ and $\theta=\pi/2$ depicted in Fig. 3 for the four different possible combinations of symmetry/antisymmetry properties on the two boundaries. The corresponding abbreviations are given in Table 1. Imposing a symmetry (respectively antisymmetry) property at a boundary on a variable ensures that this variable reaches an anti-node (respectively a node) on this boundary.

The symmetry and antisymmetry conditions are imposed through hard-wall and soft-wall boundary conditions. As a matter of fact, and as pointed out by Atkins [18], symmetry conditions on the pressure are identical to hard-wall boundary conditions. Likewise, antisymmetry conditions are identical to soft-wall boundary conditions. This may be shown by imposing on the exterior trace ϕ^+ the conditions $\mathbf{u}^+ \cdot \mathbf{n} = -\mathbf{u}^- \cdot \mathbf{n}$ and $p^+ = p^-$ (respectively $\mathbf{u}^+ \cdot \mathbf{n} = \mathbf{u}^- \cdot \mathbf{n}$ and $p^+ = -p^-$). It results that $[\mathbf{A}_j n_j]^- (\phi^+ - \phi^-) = \mathbf{M}(\beta = 1) \phi^-$ (respectively $[\mathbf{A}_j n_j]^- (\phi^+ - \phi^-) = \mathbf{M}(\beta = -1) \phi^-$).

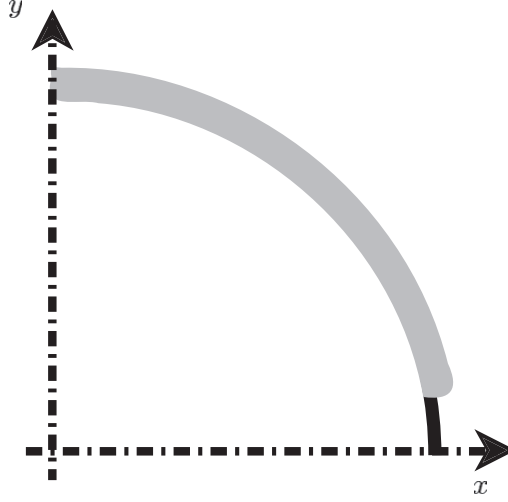


Fig. 3. Computational domain.

Table 1

Notations used for the symmetry properties of the computed modes.

y-axis symmetry property on p	x-axis symmetry property on p	Abbreviation
Symmetry	Symmetry	SS
Symmetry	Antisymmetry	SA
Antisymmetry	Symmetry	AS
Antisymmetry	Antisymmetry	AA

The discontinuous Galerkin formulation given by Eq. (7) may be written under the global matrix form: $\mathbf{DX} = -ik\mathbf{EX}$. This eigenvalue problem is solved with `SLEPC` [19] by means of the Krylov-Schur method and shift-invert spectral transformation. Thus, a computation does not give the full spectrum but only a few eigenvalues around a shift σ .

The method is suitable to handle any geometry since the mesh may be structured or not and may be refined locally (see Section 4.3 below).

4. Validations

4.1. Uniformly lined duct

This section deals with the no-flow ($M_0 \equiv 0$) case where the duct is uniformly lined ($\theta_s = 0$). The wavenumber $k_{m,n}$ of the mode (m,n) (i.e. of azimuthal order m and radial order n) admits an analytical solution $k_{m,n} = \pm \sqrt{\omega^2 - Y_{m,n}^2}$ where $Y_{m,n}$ is given by the n th solution of the equation

$$\frac{J'_m(X)}{J_m(X)} X = \frac{i\omega}{Z} \quad (8)$$

where J_m is the m -th order ordinary Bessel function of the first kind. The eigenfunction of the mode (m,n) is then:

$$p_{m,n}(r, \theta) = A^+ J_m(Y_{m,n} r) e^{im\theta} + A^- J_m(Y_{m,n} r) e^{-im\theta} \quad (A^+, A^-) \in \mathbb{C}^2 \quad (9)$$

A detailed analysis and a method to find the solutions are given in [20]. At high frequencies, representative of the turbofan acoustics, the radial modes $n=1$ are so-called surface waves. As pointed out by Rienstra [20], they are modes which exist only in the vicinity of the liners. The radial modes $n=2,3,4,\dots$ are genuine acoustic modes.

The angular frequency $\omega = 30$ is chosen with $Z = 2 + i$. The values correspond to those chosen in [5] and Brambley et al. [6], and are relevant for the study of duct acoustics modelling engine nacelles. Same values will be imposed in Section 5 when studying the effects of the rigid splices.

The computations are done for the four cases SS, AS, SA, AA. Numerical results represented by open circles in Fig. 4 are superimposed to the analytic ones. The upper branch corresponds to surface waves ($n=1$) and the other branches correspond to acoustic modes ($n=2,3,4,\dots$). The lines corresponding to each branch are plotted by linking together the analytical eigenvalues corresponding to each radial mode. On each branch, the mode the most on the right is an axisymmetric mode ($m=0$), the second mode is $m=1$, the third mode is $m=2$, and so on and so forth.

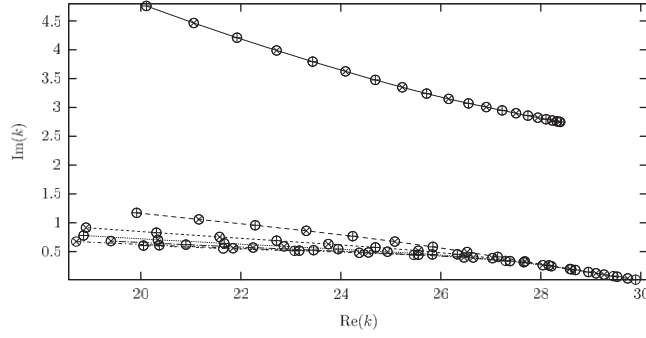


Fig. 4. Comparison between the numerical solutions and the analytical solutions ($\omega = 30$; $Z = 2 + i$, $M_0 = 0$). Theoretical solution: odd (\times) and even ($+$) azimuthal mode. Numerical solution: \circ ; — : $n=1$; - - - : $n=2$; : $n=3$; ······ : $n=4$; - · - · : $n=5$; - - - : $n=6$; - · - · : $n=7$.

Table 2

Simplifications on the solution equation (9) imposed by the boundary conditions (A is an arbitrary complex amplitude).

Configuration	Solution $p(r, \theta)$	Parity of m
SS	$AJ_m(Y_{m,n}r)\cos(m\theta)$	Even
SA	$AJ_m(Y_{m,n}r)\sin(m\theta)$	Odd
AS	$AJ_m(Y_{m,n}r)\cos(m\theta)$	Odd
AA	$AJ_m(Y_{m,n}r)\sin(m\theta)$	Even

When imposing the boundary conditions of the AA, AS, SA and SS configurations, the solution given by Eq. (9) is simplified. The simplifications are given in Table 2.

The 2D eigenfunctions obtained for an AA configuration correspond to phase-shifted SS eigenfunctions and therefore the eigenvalues of the AA and SS configurations are the same. For example, in Fig. 5 is plotted the real part of the pressure for the analytical mode (2,2). It may be seen as an SS mode regarding the thick dashed straight lines or it may be seen as an AA mode considering the straight solid lines. Similarly, eigenvalues obtained in the SA and AS configurations are identical and the eigenfunctions are just phase-shifted.

Consequently the axisymmetric azimuthal modes $m=0$ correspond to SS modes, as expected, while even azimuthal modes correspond to both AA and SS modes and odd azimuthal modes correspond to both AS and SA modes.

A very good agreement between the numerical and analytical solutions is observed since for the eigenvalues plotted in Fig. 4 the relative error goes from 1.1×10^{-7} to 1.8×10^{-5} . The present approach with the corresponding developed stability code is thus validated for no flow.

4.2. Lined duct with splices

4.2.1. No flow case

Bi [3] calculated eigenmodes in a non-uniformly lined circular duct without flow. The calculations were conducted by means of the multimodal method: the solution was expanded in terms of eigenvectors of the rigid duct case. Among different configurations of non-uniformly lined duct, Bi considered the lined duct with two rigid splices diametrically opposed. The calculations were performed for $\omega = 31.26$, $Z = 2 + i$, $M_0 = 0$ and $\theta_s = 0.15$. The nine least damped eigenmodes are given.

The same configuration has been calculated with the present numerical method, results have been presented in [21]. A good agreement on the eigenvalues is obtained considering the number of digits given by Bi and a qualitative good agreement on the shape of the eigenfunctions is found. Computations have been done on three meshes of 1194, 10 380, and 19 656 triangles, respectively numbered mesh one to three. The mesh convergence has been evaluated by considering the residuals (i.e. the relative change in the value of a wavenumber between two computations) for the nine wavenumbers given by Bi. The largest residual found by comparing the wavenumbers obtained with mesh one and mesh two is 3.87×10^{-6} and 9.57×10^{-6} when comparing the eigenvalues obtained on mesh two and mesh tree. Considering the precision imposed on the Krylov-Schur computation, these results show that convergence has been reached.

4.2.2. Flow case

Brambley et al. [6] proposed a method based on a Fourier series expansion for the computation on any geometry in the presence of axial sheared flows. In order to validate further the present method in the presence of flow, qualitative comparisons are done with spectra shown by Brambley et al. [6]. First a parabolic sheared flow defined in Eq. (10) is

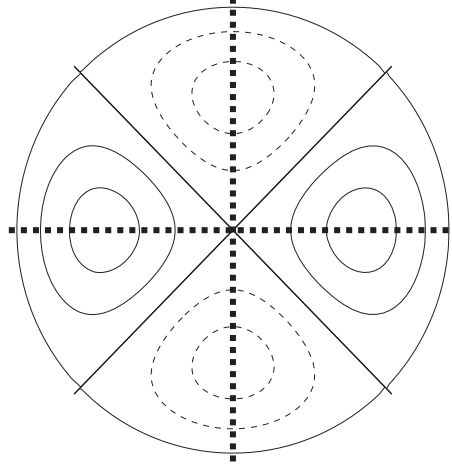


Fig. 5. Contours of $\text{Re}(p)$ for the mode (2,2). Solid contours are positive, dashed contours are negative.

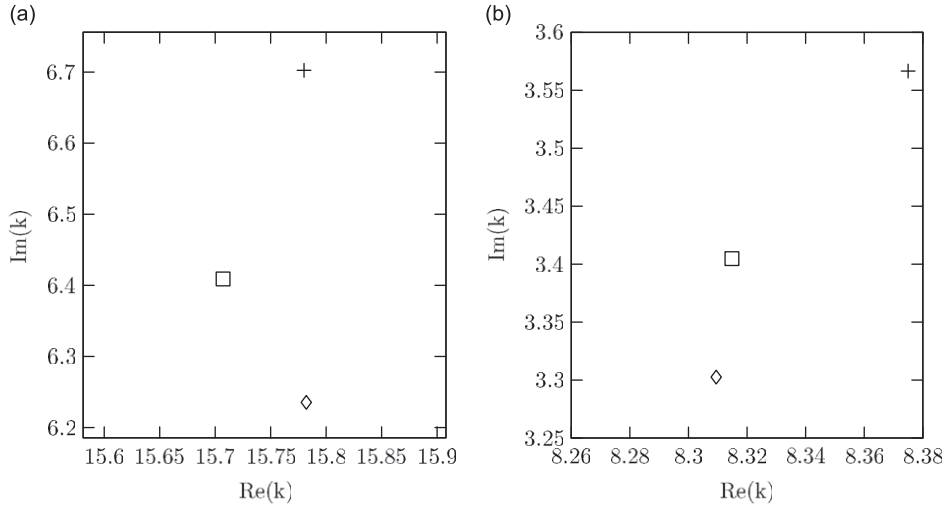


Fig. 6. Validation cases: $\theta_s = 0.1$, $\omega = 31$, $Z = 2 + i$, $M = 0.5$: (a) Parabolic sheared flow defined by Eq. (10). (b) Thin sheared flow defined by Eq. (11) with $\delta = 10^{-3}$. +: Unspliced duct ($\theta_s = 0$); \square : SS mode; \diamond : AA mode.

considered:

$$\frac{M_0(r)}{M} = 1 - r^2 \quad (10)$$

Then the thin sheared boundary flow defined by Rienstra and Vilenski [22], see Eq. (11) is used:

$$\frac{M_0(r)}{M} = \tanh\left(\frac{1-r}{\delta}\right) + \left(1 - \tanh\left(\frac{1}{\delta}\right)\right) \left(\frac{1 + \tanh\left(\frac{1}{\delta}\right)}{\delta} r + 1 + r\right) (1-r) \quad (11)$$

In Fig. 6(a) and (b) are shown small regions of the spectra obtained with these two flows for $\omega = 31$, $\theta_s = 0.1$, $Z = 2 + i$, $M = 0.5$ and $\delta = 10^{-3}$ as in Ref. [6]. Although being able to compute all the modes, Brambley et al. focused on the modes satisfying the condition $p(1, \theta + \pi) = p(1, \theta)$ and therefore the calculations for the spliced duct have been conducted for the AA and SS modes only. A qualitative good agreement is obtained with [6, Fig. 13(b) and Fig. 12(c)], which correspond to an azimuthal order $m = 24$ for the unspliced mode.

Results presented in this section have shown that the developed numerical method is suitable for the computation of acoustic modes on any geometric configuration with any arbitrary sheared mean flow. In the next section, the ability of the method to compute robustly the different components of the perturbation vector in the vicinity of the lining discontinuities will be addressed.

4.3. Convergence properties

In this section is presented a mesh convergence analysis as performed in [21]. Computations have been performed without flow on a rectangular rigid duct of height H (the length of reference) and of width $L=AH$ (A is the aspect ratio) with $\omega = \omega^*H/a_0 = 2.35$ (ω^* is the dimensional angular frequency). The geometry is meshed by repeating the mesh pattern represented in Fig. 7. Two meshes have been generated: the first one is defined by $\Delta x = \Delta y = L/50$ and the second one is constructed with $\Delta x = \Delta y = L/75$.

For this trivial configuration, the analytical solution for a mode (m,n) exhibiting $m/2$ wavelengths along y and $n/2$ wavelengths along x is given by $k_a = \pm \sqrt{\omega^2 - (n\pi A)^2 - (m\pi)^2}$. The relative error on the eigenvalues, defined as $|k - k_a|/|k_a|$, is computed for modes $(m,0)$ (respectively for modes $(0,n)$) and plotted against $\lambda/h = \lambda_y/\Delta y = 2H/(m\Delta y)$ (respectively against $\lambda/h = \lambda_x/\Delta x = 2L/(n\Delta x)$) in Fig. 8. The relative error goes from 4.04×10^{-12} for $\lambda/h = 150$ to 3.18×10^{-4} for $\lambda/h = 5.6$ and a fifth-order rate of convergence is observed.

For spliced geometry studies in this paper, an unstructured mesh with local refinement is considered (see Fig. 9). The mesh generator GMSH is used [23], the refinement is achieved by defining an attractor point at the lining discontinuity. In practice, the mesh used in the uniformly lined case is reused and the attractor point is defined such as there are 20 elements on the spliced area. The mesh is then refined until mesh convergence is observed on the eigenvalues. The refinement strategy could be optimised by implementing an *a posteriori* error estimation for local mesh adaptivity [8].

In Fig. 10 is plotted the computation time as a function of the size N of the matrices (if N_T is the number of triangles in the mesh then $N = 24N_T$). Serial computations have been performed on an Intel Xeon Woodcrest 5160. Displayed times correspond to computations performed with or without flow and in spliced or unspliced configuration. In these computations, where the maximum dimension of the subspace in the Krylov-Schur method is 80, between 30 and 80 eigenvalues are found. $O(N^2)$ time complexity is observed. Shift-invert spectral transformation in the Krylov-Schur method requires to solve a linear system at each iteration. This is done by means of a direct solving (sparse LU factorisation). Computations could be speeded up by using an iterative solver together with an appropriate preconditioner and parallel computing.

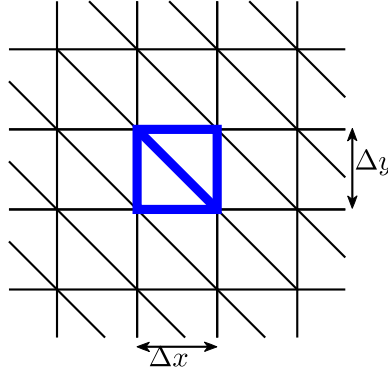


Fig. 7. Mesh pattern used for the mesh convergence analysis.

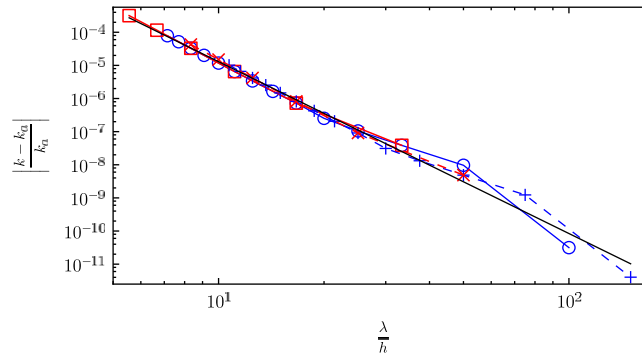


Fig. 8. Effect of the mesh resolution on the accuracy—relative error on the eigenvalues $|(k - k_a)/k_a|$ against λ/h . \circ —: mesh #1, modes $(0,n)$; $+$ —: mesh #2, modes $(0,n)$; \square —: mesh #1, modes $(m,0)$; \times —: mesh #2, modes $(m,0)$; —: $|(k - k_a)/k_a| \sim (\lambda/h)^{-5.19}$.

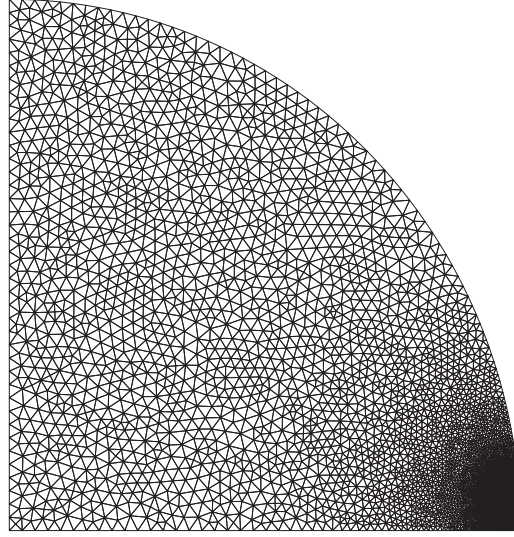


Fig. 9. Example of unstructured mesh refined at the liner-splice discontinuity.

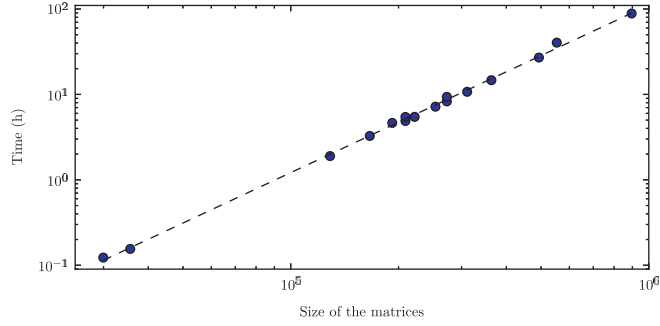


Fig. 10. Speed of convergence: computation time T as a function of the size of the matrices N (●: Computation time; - - - -: $T \sim N^{1.96}$).

5. Investigation of discontinuity effects

In the following, the splice width is fixed such as $\theta_s = 0.05$ (i.e. the unlined section represents 3.18 percent of the duct circumference), $\omega = 30$ and $Z = 2 + i$, as chosen in [6, Section 6.5] when studying localised modes and in Section 4.1 when studying the unspliced case. In all sections but Sections 5.3 and 5.5, no mean-flow is considered ($M_0 \equiv 0$). Calculations have been performed for the SS, AA, AS and SA cases.

5.1. Shape of the eigenfunctions especially at the wall

In this section, the spliced eigenfunctions are analysed. In particular, the behaviour of the eigenfunctions associated to the spliced modes originating as the unspliced mode ($m=16, n=2$) is investigated. The azimuthal wavenumber m being even, these modes are AA and SS modes. The corresponding unspliced eigenvalue is $k = 19.92 + 1.17i$ and the spliced eigenvalues are $k_{AA} = 19.89 + 1.17i$ and $k_{SS} = 19.85 + 1.11i$.

Eigenfunctions $\text{Re}(p)$ of the unspliced mode (16,2) and of its corresponding AA and SS spliced modes are shown in Fig. 11. The SS eigenfunction shows more discrepancies with the unspliced mode than the AA eigenfunction especially near the splice.

Fig. 12 shows the absolute value of the radial velocity component at the wall for the modes SS and AA originating as the unspliced mode (16,2). The whole interval $\theta \in [0, \pi/2]$ has not been plotted, since the effects of the splice are mainly noticeable for small θ . Except at the splice, the radial velocity of the AA mode is in rather good agreement with the unspliced exact solution, while for small θ even qualitatively the radial velocity of the SS mode is not comparable with the analytical unspliced solution.

Figs. 13 and 14 are equivalent to Fig. 12 but for the pressure and the azimuthal velocity component respectively. As far as the pressure is concerned, on the lined section $\theta \in [\theta_s, \pi/2]$, the conclusions are similar to those reported for the radial velocity component owing to the impedance boundary condition $Zu_r = p$. Moreover, the pressure eigenfunction of the AA

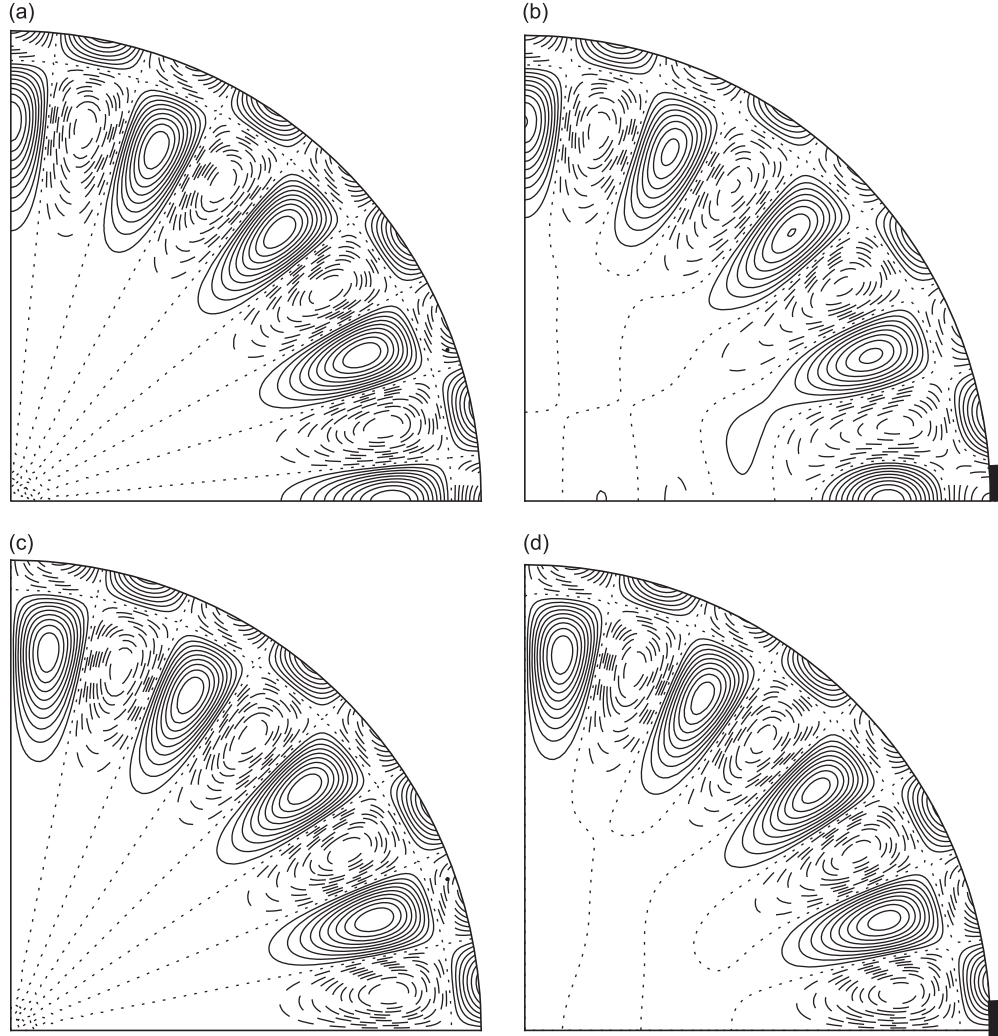


Fig. 11. Contours of $\text{Re}(p)$ for the unspliced mode (16,2) (a), (c) and for its corresponding spliced SS mode (b) and AA mode (d). The splice is represented by the thick line ($\theta_s = 0.05$). Contours are spaced at $\{0.1, 0.2, \dots, 0.9\} \times \max|p|$, solid contours are positive, dashed contours are negative and dotted contours are zero-contours.

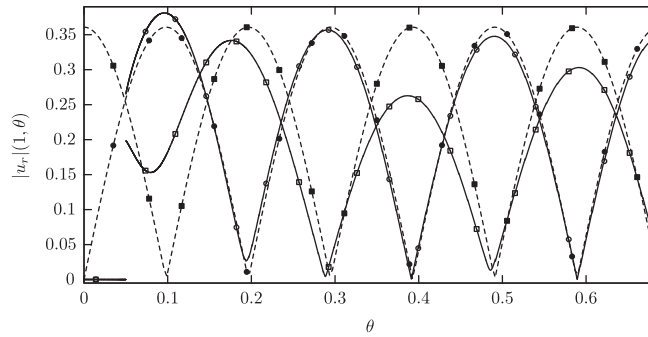


Fig. 12. Absolute value of the radial velocity component at the duct wall $|u_r|(1, \theta)$ for the modes SS ($-\square-$) and AA ($-\circ-$) originating as the unspliced mode (16,2) ($-\blacksquare-$) and ($-\bullet-$). The rigid splice is located between $\theta = 0$ and $\theta = \theta_s = 0.05$.

mode is in rather good agreement with the unspliced solution even at the splice. Regarding the azimuthal velocity component, it presents a peak at the impedance discontinuity. Except on and near the splice, the conclusions are similar to those on the radial velocity component and on the pressure component when comparing the AA and SS solutions with the

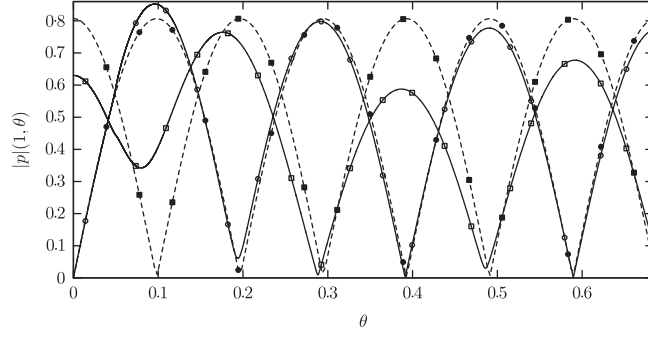


Fig. 13. Absolute value of the azimuthal velocity component at the duct boundary for the modes SS (—□—) and AA (—○—) originating as the unspliced mode (16,2) (—■—) and (—●—). The rigid splice is located between $\theta = 0$ and $\theta = \theta_s = 0.05$.

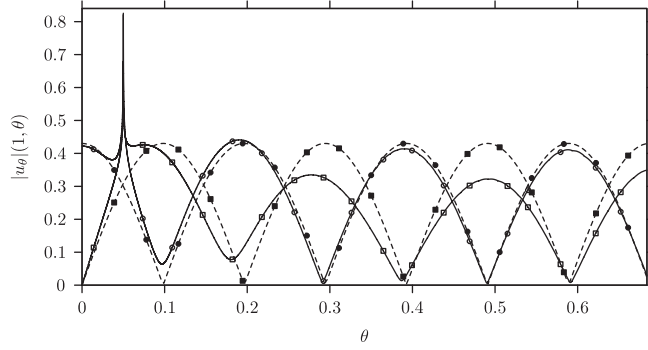


Fig. 14. Absolute value of the pressure at the duct boundary for the modes SS (—□—) and AA (—○—) originating as the unspliced mode (16,2) (—■—) and (—●—). The rigid splice is located between $\theta = 0$ and $\theta = \theta_s = 0.05$.

exact solution. Refining the mesh at the lining discontinuity leads to higher peaks both for the AA and SS modes, leading us to believe that the azimuthal velocity is tending towards infinity at the wall impedance jump.

5.2. Discussion about singularities

Figs. 12 and 14 show that $u_r(1, \theta)$ is discontinuous at $\theta = \theta_s$ and $u_\theta(1, \theta)$ seems to tend towards infinity as θ tends towards θ_s . Although no complete analytical study is possible to characterise the solution at the boundaries, a few results may be found analytically.

The most straightforward analytical investigation concerns the radial acoustic velocity component. At the joint between the rigid splice and the liner, the boundary condition written in cylindrical coordinates is jumping from $u_r(1, \theta_s^-) = 0$ to $u_r(1, \theta_s^+)Z = p(1, \theta_s^+)$, which explains the discontinuity on the radial velocity noticeable in Fig. 12.

As far as the azimuthal acoustic velocity component is concerned, combining the momentum equations in cylindrical coordinates on \mathbf{e}_θ and on \mathbf{e}_r yields

$$\partial_r(r u_\theta) = \partial_\theta u_r \quad (12)$$

Radial component u_r being discontinuous at the hard–soft wall transition, singular properties are expected on $\partial_r(r u_\theta)$ at this position. Although it is not possible to conclude directly on u_θ from Eq. (12), it helps understanding the singular behaviour shown in Fig. 14.

Refining the mesh increases the peak on the azimuthal velocity at the hard–soft wall junction only. Moreover the singular behaviour on the eigenfunctions seems to take place at the wall impedance jump only. In Fig. 15 are plotted $|u_r|$ and $|u_\theta|$ at $r = 0.999$ as functions of θ for three different meshes. The first mesh is coarse (1484 triangles), the second one has 8711 triangles, the third mesh is much refined (37 294 triangles). It appears that for both the radial velocity component and the azimuthal velocity component, no singular behaviour is observed and no major discrepancies are noticeable between the results obtained with the different meshes.

It can be also shown that the jump on the radial velocity at $\theta = \theta_s$ and $r = 1$ (see Fig. 12) remains constant when refining the mesh. This shows the ability of the discontinuous Galerkin method to catch correctly the discontinuity on u_r . Actually, as long as the inner edges of the mesh are perpendicular to the domain boundary at the lining discontinuities, the jump in u_r does not lead to numerical problems. Indeed, as pointed out by Cockburn [24], it is obvious in Eq. (7) that the residual on an element depends strongly on the jump $\phi^+ - \phi^-$. More precisely, with or without flow, the integral of the residual on an

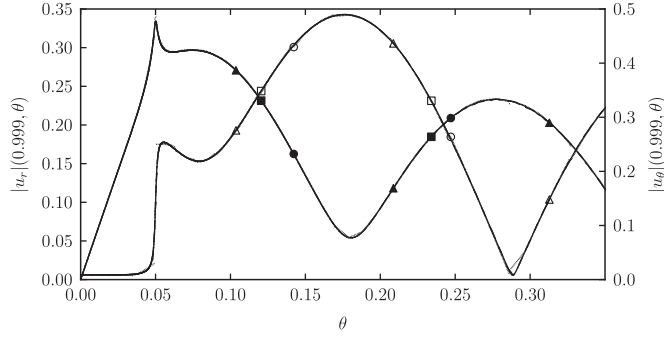


Fig. 15. Absolute value of the radial velocity component $|u_r|$ (empty symbol) and of the azimuthal velocity component $|u_\theta|$ (filled symbol) at $r = 0.999$ as functions of θ . The solid line with triangle markers corresponds to the mesh with 37 294 triangles, the dashed line with square markers corresponds to the mesh with 8711 triangles and the dotted line with circle markers correspond to the mesh with 1484 triangles.

element depends linearly on the integral on the bounding inner edges of the term:

$$[\mathbf{A}_j n_j]^-(\boldsymbol{\varphi}^+ - \boldsymbol{\varphi}^-) \cdot \boldsymbol{\psi}_m = -\frac{1}{2} \begin{pmatrix} n_x(\mathbf{u}^+ \cdot \mathbf{n} - \mathbf{u}^- \cdot \mathbf{n}) - n_x(p^+ - p^-) \\ n_y(\mathbf{u}^+ \cdot \mathbf{n} - \mathbf{u}^- \cdot \mathbf{n}) - n_y(p^+ - p^-) \\ 0 \\ -(\mathbf{u}^+ \cdot \mathbf{n} - \mathbf{u}^- \cdot \mathbf{n}) + p^+ - p^- \end{pmatrix} \cdot \boldsymbol{\psi}_m. \quad (13)$$

Hence, the local residual depends on the pressure and normal velocity jumps at the edges of the local element. If the lining discontinuity point corresponds to the end point of an internal edge between two triangles and if this edge is perpendicular to the computational domain boundary $\partial\Omega_h$, then the velocities normal to this edge $\mathbf{u}^+ \cdot \mathbf{n}$ and $\mathbf{u}^- \cdot \mathbf{n}$ corresponds purely to u_θ . The meshes used in the computations satisfy this condition and therefore, the local residuals on the two triangles bordered by this edge are not affected by the radial velocity jump but only by the azimuthal velocity and pressure jumps.

5.3. Symmetry conditions and discrepancies with the uniformly lined duct configuration

As seen in Section 5.1 in Figs. 11–14, the eigenfunction of the mode AA is in better agreement with the corresponding unspliced solution (mode (16,2)) than the eigenfunction of the mode SS. Brambley et al. [6] derived an asymptotic method to compute spliced eigenmodes for $\theta_s \ll 1$. They showed that for a mode of azimuthal order m the perturbation to Fourier modes of order n is $O(\theta_s)$ for $n \gg m$. Moreover, for $(m\theta_s) \ll 1$, they have demonstrated that the unspliced wavenumber perturbation by the splice is $O(\theta_s)$ for modes with $\cos(m\theta)$ (i.e. AS and SS modes) dependence while it is $O(\theta_s^3)$ for unspliced modes with $\sin(m\theta)$ (i.e. AA and SA modes) dependence. This difference in spliced effect depending on the mode symmetry is illustrated in this section by considering the acoustic kinetic energy, first without flow. It is then shown that similar results are obtained with flow.

Consider the linearised Euler equations written in cylindrical coordinates with mean flow. The momentum equations on \mathbf{e}_r , on \mathbf{e}_θ and on \mathbf{e}_z read respectively:

$$\begin{cases} i(kM_0 - \omega)u_r + \partial_r p = 0 & (a) \\ i(kM_0 - \omega)u_\theta + \frac{1}{r}\partial_\theta p = 0 & (b) \\ i(kM_0 - \omega)w + ikp + (\partial_r M_0)u_r = 0 & (c) \end{cases} \quad (14)$$

and the continuity equation is

$$i(kM_0 - \omega)p + \partial_r u_r + \frac{1}{r}u_r + \frac{1}{r}\partial_\theta u_\theta + ikw = 0 \quad (15)$$

Then, without flow ($M_0 \equiv 0$), after some manipulation the acoustic kinetic energy on the computational domain can be expressed as

$$\begin{aligned} E = \int_{\Omega_h} (|u_r|^2 + |u_\theta|^2 + |w|^2) d\Omega &= \int_{\Omega_h} \left(1 + \frac{|k|^2 - k^2}{\omega^2}\right) |p|^2 d\Omega - \frac{i}{\omega} \left[\int_0^1 u_\theta \bar{p} dr \right]_{\theta=\theta_s^-}^{\theta=\theta_s^+} + \frac{i}{\omega} \int_0^{\theta_s} u_r(1, \theta) \bar{p}(1, \theta) d\theta \\ &\quad + \frac{i}{\omega} \int_{\theta_s}^{\pi/2} u_r(1, \theta) \bar{p}(1, \theta) d\theta \end{aligned} \quad (16)$$

The overline represents the complex conjugate of the corresponding parameter.

The jump term in Eq. (16) equals zero. Indeed, it has been shown previously that the singular behaviour of the eigenfunctions is restricted to the wall location and so $(u_\theta \bar{p})(r, \theta)$ is continuous at $\theta = \theta_s$ and r such as $0 \leq r < 1$. Cancellation of this term has been checked numerically as well.

Using the impedance boundary condition in the spliced configuration, Eq. (16) becomes

$$E_{\text{spliced}} = \int_{\Omega_h} \left(1 + \frac{|k|^2 - k^2}{\omega^2} \right) |p|^2 d\Omega + \frac{i}{Z\omega} \int_{\theta_s}^{\pi/2} |p|(1, \theta)^2 d\theta \quad (17)$$

Whereas in the unspliced (i.e. uniformly lined) duct configuration, it reads

$$E_{\text{uni}} = \int_{\Omega_h} \left(1 + \frac{|k|^2 - k^2}{\omega^2} \right) |p|^2 d\Omega + \frac{i}{Z\omega} \int_{\theta_s}^{\pi/2} |p|(1, \theta)^2 d\theta + \frac{i}{Z\omega} \int_0^{\theta_s} |p|(1, \theta)^2 d\theta \quad (18)$$

If the pressure component of an unspliced mode satisfies an antisymmetry condition about the x -axis (AA or SA modes), the x -axis is a pressure node and in particular $p(1, 0) = 0$. $p(1, \theta)$ remains small between $\theta = 0$ and $\theta = \theta_s$ providing $(m\theta_s) \ll 1$. Moreover, if $\theta_s \ll 1$, the last term of Eq. (18) corresponds to the integral of a small integrand on a small domain and may thus be neglected. It follows that the spliced and the unspliced eigenpairs (k, ϕ) satisfy almost the same integral equation. As a consequence, we are likely to think that the spliced and unspliced solutions would exhibit few discrepancies. More precisely, Brambley et al. [6] showed that the perturbation to the unspliced eigenvalues is $O(\theta_s^3)$.

On the contrary, if a symmetry condition on the pressure component with respect to the x -axis is imposed, the x -axis is a pressure anti-node. As a consequence, under the assumptions $\theta_s \ll 1$ and $(m\theta_s) \ll 1$ only the domain of integration is small in the last integral term of the right-hand side of Eq. (18) and not the integrand. Brambley et al. [6] proved that the perturbation to the unspliced wavenumbers is then only $O(\theta_s)$.

With flow, the reasoning is similar. Manipulating Eqs. (14a)–(14c) and Eq. (15) yields

$$\begin{aligned} I = \int_{\Omega_h} i(kM_0 - \omega)(|u_r|^2 + |u_\theta|^2 + |w|^2) d\Omega = & - \left[\int_0^1 u_\theta \bar{p} dr \right]_{\theta=\theta_s^-}^{\theta=\theta_s^+} + \int_{\Omega_h} (i(kM_0 - \omega)|p|^2 + i(k - \bar{k})w\bar{p} + \partial_r(M_0)\bar{u}_r w) d\Omega \\ & + \int_0^{\theta_s} u_r(1, \theta)\bar{p}(1, \theta) d\theta + \int_{\theta_s}^{\pi/2} u_r(1, \theta)\bar{p}(1, \theta) d\theta \end{aligned} \quad (19)$$

For the same reasons as without flow, the jump term equals zero. Introducing the impedance boundary conditions in the spliced configuration yields

$$I_{\text{spliced}} = \int_{\Omega_h} (i(kM_0 - \omega)|p|^2 + i(k - \bar{k})w\bar{p} + \partial_r(M_0)\bar{u}_r w) d\Omega + \frac{1}{Z} \int_{\theta_s}^{\pi/2} |p(1, \theta)|^2 d\theta \quad (20)$$

In the uniformly lined duct case, it reads

$$I_{\text{uni}} = \int_{\Omega_h} (i(kM_0 - \omega)|p|^2 + i(k - \bar{k})w\bar{p} + \partial_r(M_0)\bar{u}_r w) d\Omega + \frac{1}{Z} \int_{\theta_s}^{\pi/2} |p(1, \theta)|^2 d\theta + \frac{1}{Z} \int_0^{\theta_s} |p(1, \theta)|^2 d\theta \quad (21)$$

Eqs. (20) and (21) differ only over one integral term which is exactly the same as in the no flow case. The previous reasoning holds under the assumptions $\theta_s \ll 1$ and $(m\theta_s) \ll 1$, illustrating the fact that, with or without flow, the effect of thin splices is more pronounced for modes symmetric about the splices than modes antisymmetric about them.

5.4. Effects of the splices on the spectrum

As well as the modification of the eigenfunctions by the presence of the splice, the eigenvalues of the spliced modes are affected as well. Fig. 16 provides the spectrum obtained with the SS, AA, AS and SA computations. It seems to be characteristic of a spectrum with one or several localised modes (see [5, Fig. 3(e); 6, Fig. 14(a)]). As in the unspliced case the upper branch corresponds to surface waves and the lower branches correspond to acoustic modes, however, there are now two isolated modes in the middle. They are localised modes, originating as surface waves and turning into acoustic waves when θ_s is increased. They correspond to AS and SS modes and they originate as unspliced surface waves of azimuthal order $m=1$ and $m=2$ respectively.

As far as the acoustic waves are concerned, the spectrum is similar to the spectrum obtained for the unspliced duct (see Section 4.1 and Fig. 4). In Fig. 17(a) is plotted a zoom on the acoustic waves spectrum. The unspliced (m, n) (see Section 4.1) even and odd modes eigenvalues are plotted and encircled together with their corresponding spliced modes eigenvalues. In the vicinity of an eigenvalue corresponding to an even (respectively odd) azimuthally unspliced mode lie both a SS and an AA spliced modes (respectively both a SA and an AS unspliced modes). However, on the contrary to the unspliced case, the eigenvalues obtained in the AA (respectively AS) configuration are not identical to the eigenvalues obtained in the SS (respectively SA) configuration, owing to the loss of axisymmetry. For $m=0$ only a SS spliced mode lies in the neighbourhood of the eigenvalue.

Concerning the surface waves, the conclusions are similar for $m \gtrsim 10$. In Fig. 17(b) is plotted a zoom on the part of the spectrum associated to surface waves. However, for low azimuthal order, the AA (respectively SA) modes are in the vicinity

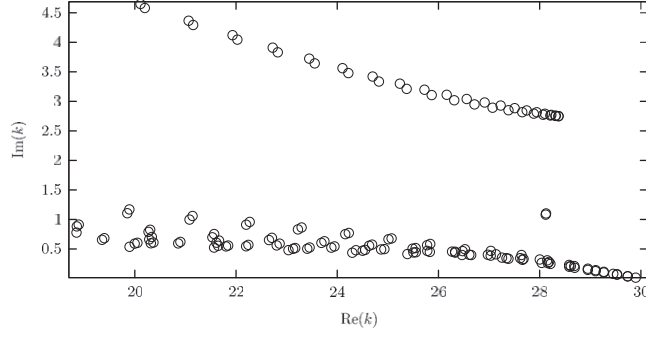


Fig. 16. Spectrum obtained for $\theta_s = 0.05$, $M_0 = 0$, $\omega = 30$ and $Z = 2 + i$.

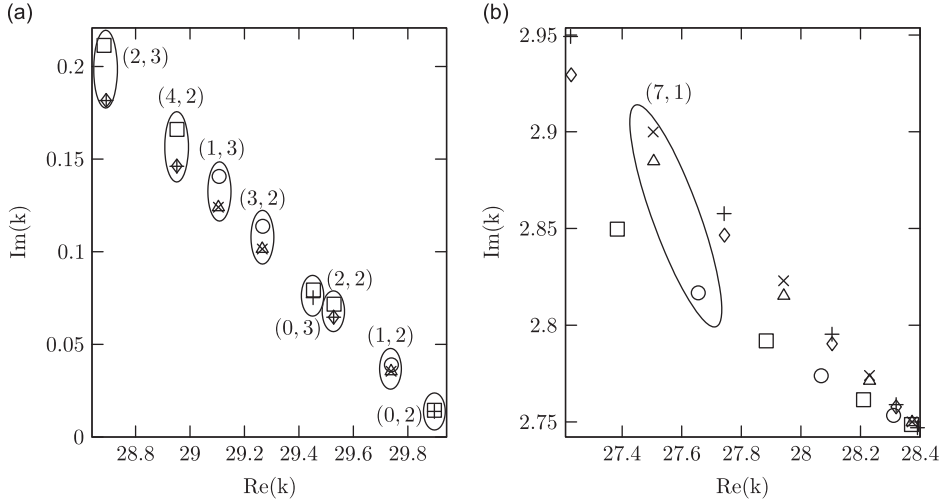


Fig. 17. Spectrum obtained for $\theta_s = 0.05$, $M_0 = 0$, $\omega = 30$ and $Z = 2 + i$: Zoom in on the right parts of the acoustic waves branches (a) and of the surface waves branch (b) (\square : SS mode; \diamond : AA mode; \circ : AS mode; \triangle : SA mode). Comparison with the odd (\times) and even ($+$) unspliced modes.

of unspliced even (respectively odd) modes but the SS (respectively AS) modes are not in the close neighbourhood. The SS and AS eigenvalues are shifted to the right as they are scattered into modes of lower azimuthal orders. For example, the unspliced mode $m=7$ is located at $k \approx 27.5 + 2.90i$, the corresponding SA mode is located at $k \approx 27.5 + 2.88i$ and the associated AS mode is located at $k \approx 27.7 + 2.82i$. Moreover, since two modes turned into localised modes, the SS mode corresponding to the unspliced surface mode $m=2$ and the AS mode associated to the unspliced surface mode $m=1$ are missing.

It has been shown in the previous section that if $(m\theta_s) \ll 1$ and $\theta_s \ll 1$, the eigenvalues of the modes satisfying an antisymmetry condition with respect to the x -axis are less modified by the splice than the eigenvalues of the modes satisfying a symmetry condition. Correspondingly, a AA (respectively SA) eigenvalue is closer to its equivalent unspliced theoretical even (respectively odd) wavenumber than the corresponding SS eigenvalue (respectively AS wavenumber). This may be observed in Fig. 17(a) and (b) for both acoustic modes and surface waves.

As far as the spatial growth rate is concerned, the surface modes in the presence of splices are less damped than their corresponding unspliced modes, owing to a smaller acoustically treated surface (see Fig. 17(b)). However, for acoustic modes, this is not true for all the modes. It seems that at low azimuthal order, the acoustic modes are more damped in the spliced case (see Fig. 17(a)) in spite of a smaller lined surface.

5.5. Presence of a parabolic sheared flow

In this section, the previous configuration ($\theta_s = 0.05$, $\omega = 30$, $Z = 2 + i$) is kept but now with a parabolic sheared flow defined by Eq. (10) with $M = 0.5$. In Fig. 18 are plotted the eigenvalues obtained with SS, AA, AS and SA computations. As for the no-flow case, there is a surface waves branch and two localised modes in addition to the least damped modes corresponding to acoustic modes and divided on different branches, depending on their radial order. Compared to the no-flow case (see Fig. 16) where the acoustic branches are almost superimposed, they are now well separated. Moreover,

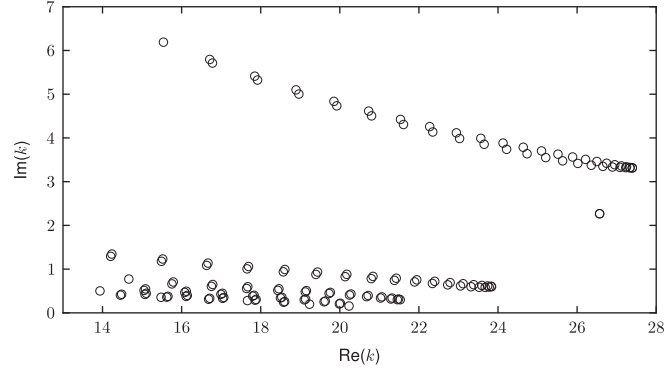


Fig. 18. Spectrum obtained for a parabolic sheared flow (defined by Eq. (10)) with $M=0.5$, $\theta_s=0.05$, $\omega=30$, $Z=2+i$.

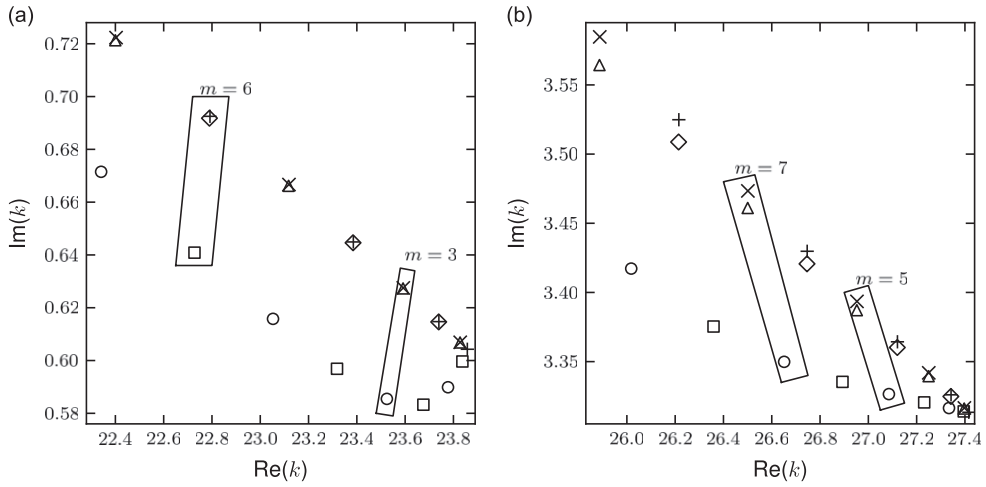


Fig. 19. Spectrum obtained for a parabolic sheared flow (defined by Eq. (10)) with $M=0.5$, $\theta_s=0.05$, $\omega=30$ and $Z=2+i$: Zoom in on the right parts of the acoustic waves branches (a) and of the surface waves branch (b) (\square : SS mode; \diamond : AA mode; \circ : AS mode; \triangle : SA mode). Comparison with the odd (\times) and even ($+$) unspliced modes.

the mean flow being a sheared flow, there is as well a continuous spectrum. The latter is not studied in this paper and not shown in Fig. 18.

In this case, the unspliced solution may not be found analytically and so the unspliced modes are computed with the method presented in this paper, although a unidimensional method would have been sufficient (the problem is axisymmetric). For the unspliced configuration, computations have been made for the SS and AS boundary conditions to obtain both the even and odd azimuthal modes. In Fig. 19(a) is shown a zoom on the right part of the first acoustic branch and in Fig. 19(b) is plotted a zoom in the right part of the surface waves branch. On both figures are shown the unspliced odd and even modes and two of them are enclosed together with their corresponding spliced mode eigenvalues. The results are similar to the no-flow case: near an azimuthally even (respectively odd) unspliced mode lie an AA mode (respectively an SA mode). In the present configuration, the eigenvalues of the acoustic modes presenting a symmetry property on the pressure with respect to x -axis (AS and SS modes) are more affected by the splice than in Section 5.4 even though the splice width θ_s is the same. Moreover, in the presence of a parabolic sheared flow profile and for the chosen parameters, all spliced modes (even acoustic modes) are less damped than their unspliced equivalents, which was not the case without flow, see Section 5.4.

Without flow (see Fig. 16) the eigenvalue corresponding to the localised SS mode was quite close to the eigenvalue associated with the localised AS mode: the relative deviation was 7.5×10^{-4} . With flow, the relative deviation is only 7.5×10^{-7} .

6. Computations on other geometries

In order to demonstrate the flexibility of the method, computations with flow in ducts of different geometries and with lining discontinuities are presented in this section. First computations are performed on a flow duct of elliptic cross-

section (Fig. 20(a)) and then on a flow duct of square cross-section (Fig. 20(b)). Thanks to the symmetry properties, computations are performed on the upper-right quarter of each domain ($0 \leq \theta \leq \pi/2$ or $x > 0$ and $y > 0$). As in the previous section, abbreviations SS, SA, AS, AA are used to designate the computations according to the symmetry properties imposed on the boundaries of the computational domain (see Table 1).

For both geometries, meshes have been refined until mesh convergence. They are shown in Fig. 21(a) and (b).

6.1. Duct of elliptic cross-section

For ground clearance reasons, large aero-engines may be “flattened”. Therefore, the understanding of sound propagation in a duct of elliptic cross-section is of particular interest [25–27]. The considered elliptic duct geometry is depicted in Fig. 20. The semi-major axis is R and the semi-minor axis is αR with $\alpha = \frac{4}{5}$. Two splices are located around $\theta = 0$ and $\theta = \pi$ and are $2\theta_s$ wide. A Poiseuille flow defined by Eq. (22) is running through the duct [28]. For both flows defined by Eqs. (10) and (22), the mean Mach number is $M_v = M/2$.

$$\frac{M_0(x,y)}{M} = 1 - x^2 - \frac{y^2}{\alpha^2} \quad (22)$$

Parameters chosen in Section 5.5 for the study of the effects of a parabolic sheared flow are kept ($\theta_s = 0.05$, $\omega = 30$, $Z = 2 + i$ and $M = 0.5$, the reference length is R). The wavenumbers obtained with SS, AA, AS and SA computations are plotted in Fig. 22. The spectrum is quite similar to the spectrum obtained in a circular duct carrying a parabolic flow (see Fig. 18). It contains eigenvalues corresponding to surfaces modes, acoustic modes and localised modes, almost at the same position as

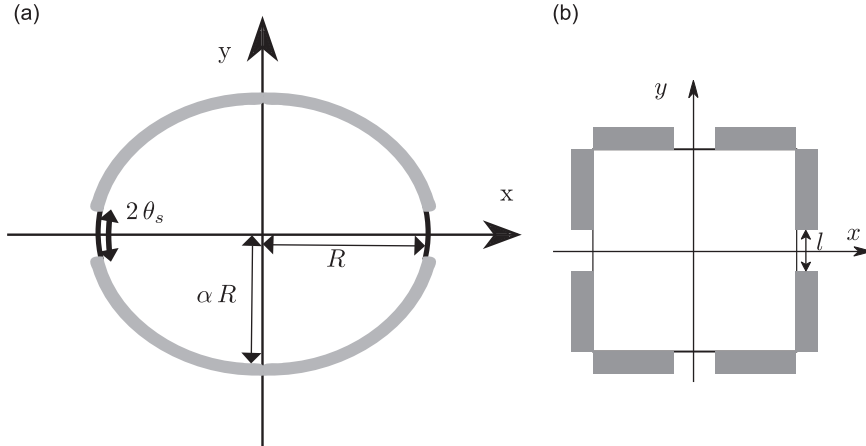


Fig. 20. Ducts with elliptic (a) and square (b) cross-section (lined walls are represented by wide grey lines).

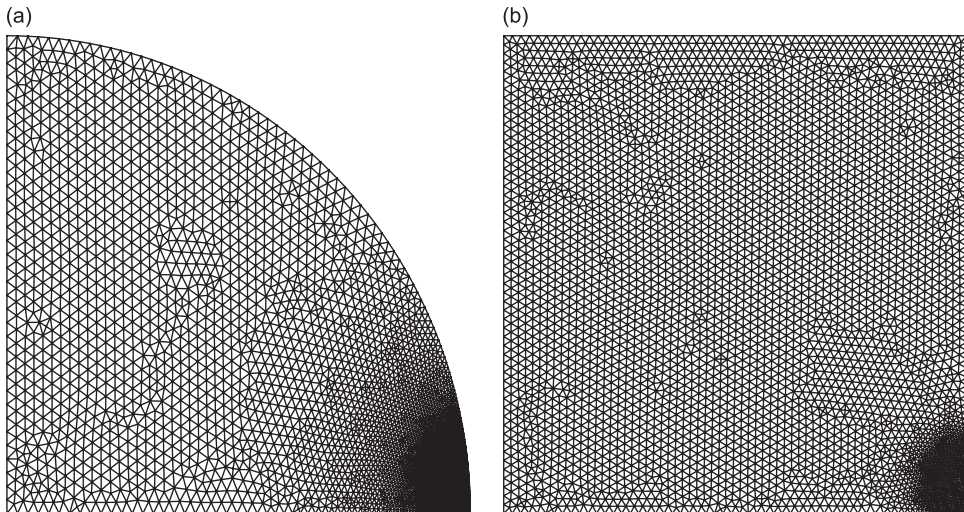


Fig. 21. Meshes used for the computations on the ducts with elliptic cross-section (a) and square cross-section (b).

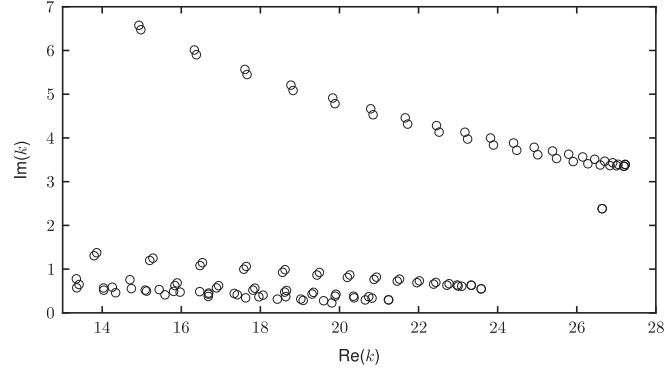


Fig. 22. Spectrum obtained for a Poiseuille flow (defined by Eq. (22)) in an elliptical duct with $M=0.5$, $\theta_s = 0.05$, $\omega = 30$, $Z=2+i$.

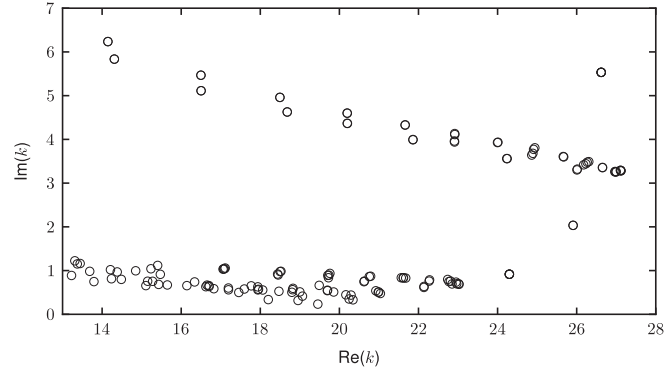


Fig. 23. Spectrum obtained for a Poiseuille flow running through a square duct partially lined with $\omega = 30$, $Z=2+i$ and a mean Mach number $M_v = 0.25$.

in the circular duct case. The relative derivation between the localised SS eigenvalue and the localised AS eigenvalue is 1.9×10^{-6} , slightly greater than in the circular duct case.

6.2. Duct of square cross-section

In this section is considered the modal analysis in a duct of square cross-section. The walls are lined except in the vicinities of the point $(L/2, 0)$ and $(-L/2, 0)$ where L is the side length and $(0, 0)$ is the square center, see Fig 20(b). The unlined areas $2l$ represent 3.18 percent of the cross-section perimeter, as in the spliced circular duct case. The square side length L has been chosen so that the area of the cross-section is the same as the area of the circle of radius R previously studied: $L = \sqrt{\pi R}$. The previous parameters are kept $\omega = 30$, $Z=2+i$, R is the reference length. A Poiseuille flow computed numerically by means of collocation method [29] is imposed such as the mean Mach number is 0.25.

In Fig. 23 are shown the eigenvalues resulting from SS, SA, AS and AA computations. The spectrum is rather similar to the spectra obtained for a circular duct and for a duct of elliptical cross-section: the modes may be classified as acoustic modes, surface modes or localised modes. There are both an SS localised mode and an AS localised mode lying about $k=25.90 + 2.03i$, the relative derivation between both wavenumbers being 8.4×10^{-9} , much smaller than for the circular and elliptical cases. The two eigenvalues lying around $k \approx 24.3 + i$ and $k \approx 26.6 + 5.54i$ correspond to modes that exist in the unspliced configuration as well.

7. Conclusion

In this paper, we derived a discontinuous Galerkin method for the computation of acoustic modes in a lined flow duct. The formulation is suitable for arbitrary axial sheared flow on any geometries since unstructured meshes may be used. Moreover, the method may be easily extended to more complex flows, for example with a swirl component or with a density gradient, by simply adding terms in the matrices \mathbf{A}_x , \mathbf{A}_y , \mathbf{B} of the linearised Euler equations (Eq. (1)). All the configurations analysed in this paper present symmetry properties with respect to the x - and y -axes. Therefore, to reduce the numerical costs, the computations have been performed on a quarter of domain by imposing successively symmetry and anti-symmetry boundary conditions on the resulting boundaries.

The no-flow case of an infinite uniformly lined duct has first been considered for validation purpose given that acoustic and surface waves may be computed analytically for this problem [20]. Good agreements have been observed and

the symmetry or antisymmetry properties of the eigenfunctions have been related to the parity of the azimuthal wavenumber m .

The method has then been employed to compute acoustic modes in infinite lined ducts with rigid splices. Satisfactory comparisons have been obtained with results given in Ref. [3] for the no-flow case and with results given in Ref. [6] for sheared flows with parabolic boundary layer profile or thin boundary layer profile with parameters representative of an engine intake. Numerical performances of the method have been evaluated by analysing the influence of the mesh refinement on the accuracy and by studying the speed of convergence of the method.

Finally, a thorough investigation of a small splice effect has been conducted by taking the same parameters as when studying the uniformly lined case. The discontinuous Galerkin method presents a robust behaviour in the vicinity of the lining discontinuities and gives an insight into the behaviour of the eigenfunctions at the joint between the splice and the lining. It turns out that the pressure, which is the only component of the acoustic perturbation involved in the previous studies on lining discontinuities in a duct (through the Pridmore-Brown equation), although being much more regular than the radial and azimuthal velocity components of the perturbation, has an infinite azimuthal derivative at the hard-soft wall transition. This singularity on the acoustic pressure azimuthal derivative is related to the infinite behaviour on the azimuthal velocity component at this position. Finally, the radial velocity component presents a finite jump.

For small splices ($\theta_s \ll 1$) and for $(m\theta_s) \ll 1$, Brambley et al. [6] have proved that the magnitude of the unspliced wavenumber perturbation induced by the splice is $O(\theta_s)$ for modes satisfying a symmetry condition about the x -axis while it is $O(\theta_s^2)$ for modes satisfying an antisymmetry condition. This was illustrated in this paper by deriving an integral formulation of the linearised Euler equations. The effect of the imposed symmetry conditions on the spliced-induced perturbation to the unspliced eigenmodes has been observed numerically as well, by comparing spliced and unspliced eigenfunctions of the mode ($m=16, n=2$) as well as spliced and unspliced spectra. As found by Bi et al. [5] and Brambley et al. [6], it was noticed that all the modal solutions have an unspliced equivalent although the method employed in this paper is completely different. Finally, the flexibility of the method was demonstrated by computing the eigenmodes in spliced ducts of cylindrical, square and elliptical cross-sections with a sheared Poiseuille flow.

Acknowledgements

Lucas Pascal's PhD work is funded by the "Direction Générale de l'Armement" (DGA) which is gratefully acknowledged. Christophe Peyret and Philippe Delorme from Onera (DSNA) are gratefully acknowledged for providing an early version of the CAA solver `SPACE` as well as Julien Primus from Onera (DMAE) for fruitful discussions.

References

- [1] G.W. Bielak, J.W. Premo, A.S. Hersh, Advanced Turbofan Duct Liner Concepts, Technical Report, NASA Langley, 1999.
- [2] M. Wright, Hybrid analytical/numerical method for mode scattering in azimuthally non-uniform ducts, *Journal of Sound and Vibration* 292 (3–5) (2006) 583–594.
- [3] W. Bi, Calculations of modes in circumferentially nonuniform lined ducts, *Journal of the Acoustical Society of America* 123 (5) (2008) 2603–2612.
- [4] G. Gabard, R. Astley, A computational mode-matching approach for sound propagation in three-dimensional ducts with flow, *Journal of Sound and Vibration* 315 (4–5) (2008) 1103–1124.
- [5] W. Bi, V. Pagneux, D. Lafarge, Y. Aurégan, Trapped modes at acoustically rigid splices, *AIAA/CEAS Aeroacoustics Conference 2009-3105*, AIAA, Miami, FL, 2009.
- [6] E.J. Brambley, A.M.J. Davis, N. Peake, Eigenmodes of lined flow ducts with rigid splices, *Journal of Fluid Mechanics* 690 (2012) 399–425.
- [7] P. Mustafi, J. Astley, R. Sugimoto, A computational study of the effects of liner damage on zero-splice turbofan intake liners, *18th AIAA/CEAS Aeroacoustics Conference*, 2012.
- [8] A. Cliffe, E. Hall, P. Houston, Adaptive discontinuous Galerkin methods for eigenvalue problems arising in incompressible fluid flows, *SIAM Journal on Scientific Computing* 31 (6) (2009) 4607–4632.
- [9] P. Delorme, P. Mazet, C. Peyret, Y. Ventribout, Computational aeroacoustics applications based on a discontinuous Galerkin method, *Comptes Rendus Mécanique* 333 (9) (2005) 676–682.
- [10] W. Bi, V. Pagneux, D. Lafarge, Y. Aurégan, Modelling of sound propagation in a non-uniform lined duct using a multi-modal propagation method, *Journal of Sound and Vibration* 289 (4–5) (2006) 1091–1111.
- [11] S.W. Rienstra, Acoustic scattering at a hardsoft lining transition in a flow duct, *Journal of Engineering Mathematics* 59 (2007) 451–475.
- [12] E.J. Brambley, Low-frequency acoustic reflection at a hardsoft lining transition in a cylindrical duct with uniform flow, *Journal of Engineering Mathematics* 65 (2009) 345–354.
- [13] K. Ingard, Influence of fluid motion past a plane boundary on sound reflection, absorption, and transmission, *Journal of the Acoustical Society of America* 31 (7) (1959) 1035–1036.
- [14] M. Myers, On the acoustic boundary condition in the presence of flow, *Journal of Sound and Vibration* 71 (3) (1980) 429–434.
- [15] E.J. Brambley, Fundamental problems with the model of uniform flow over acoustic linings, *Journal of Sound and Vibration* 322 (2009) 1026–1037.
- [16] E. Brambley, A well-posed boundary condition for acoustic liners in straight ducts with flow, *AIAA Journal* 49 (6) (2011) 1272–1282.
- [17] J.S. Hesthaven, T. Warburton, *Nodal Discontinuous Galerkin Methods: Algorithms, Analysis, and Applications*, 1st edn. Springer Publishing Company, Incorporated, 2007.
- [18] H.L. Atkins, Continued Development of the Discontinuous Galerkin Method for Computational Aeroacoustic Applications, *Computational Aeroacoustic Applications*, AIAA Paper, 97-1581, 1997.
- [19] V. Hernandez, J.E. Roman, V. Vidal, SLEPC: a scalable and flexible toolkit for the solution of eigenvalue problems, *ACM Transactions on Mathematical Software* 31 (3) (2005) 351–362.
- [20] S.W. Rienstra, A classification of duct modes based on surface waves, *Wave Motion* 37 (2) (2003) 119–135. ISSN 0165-2125.
- [21] L. Pascal, E. Piot, G. Casalis, Discontinuous Galerkin method for acoustic modes computation in lined ducts, *18th AIAA/CEAS Aeroacoustics Conference*, Colorado Springs, USA, 2012.

- [22] S.W. Rienstra, G.G. Vilenski, Spatial instability of boundary layer along impedance wall, *AIAA/CEAS Aeroacoustics Conference 2008-2932*, Vancouver, Canada, 2008.
- [23] C. Geuzaine, J.-F. Remacle, Gmsh: a three-dimensional finite element mesh generator with built-in pre- and post-processing facilities, *International Journal for Numerical Methods in Engineering* 79 (11) (2009) 1309–1331.
- [24] B. Cockburn, Discontinuous Galerkin methods, *ZAMM—Journal of Applied Mathematics and Mechanics/Zeitschrift für Angewandte Mathematik und Mechanik* 83 (11) (2003) 731–754.
- [25] N. Peake, A.J. Cooper, Acoustic propagation in ducts with slowly varying elliptic cross-section, *Journal of Sound and Vibration* 243 (3) (2001) 381–401.
- [26] J.M.G.S. Oliveira, P.J.S. Gil, Propagation of sound in ducts with elliptical cross-section and lined walls, *39th International Congress and Exposition on Noise Control Engineering: Inter-Noise 2010*, SPA, 2010.
- [27] M. Willatzen, L.C. Lew Yan Voon, Flow-acoustic properties of elliptic-cylinder waveguides and enclosures, *Journal of Physics: Conference Series* 52 (2006) 1–13.
- [28] T.C. Papanastasiou, G.C. Georgiou, A.N. Alexandrou, *Viscous Fluid Flow*, CRC Press, 1999.
- [29] R. Peyret, *Spectral Methods for Incompressible Viscous Flows*, Springer Verlag, Heidelberg, 2002.